*Astronomy & Astrophysics* manuscript no.
(will be inserted by hand later)



# High resolution X-ray spectroscopy of $\zeta$ Puppis with the XMM-Newton Reflection Grating Spectrometer

S. M. Kahn[1], M. A. Leutenegger[1], J. Cottam[1], G. Rauw[2⋆], J.-M. Vreux[2], A. J. F. den Boggende[3], R. Mewe[3], and M. Güdel[4]

[1] Department of Physics and Columbia Astrophysics Laboratory, Columbia University, 550 West 120th Street, New York, NY 10027, USA
[2] Institut d'Astrophysique et de Géophysique de l'Université de Liège, 5, Avenue de Cointe, B-4000 Liège, Belgium
[3] Space Research Organization of the Netherlands, Sorbonnelaan 2, 3548 CA, Utrecht, The Netherlands
[4] Laboratory for Astrophysics, Paul Scherrer Institute, Würenlingen and Villigen, 5232 Villigen PSI, Switzerland

the date of receipt and acceptance should be inserted later

**Abstract.** We present the first high resolution X-ray spectrum of the bright O4Ief supergiant star $\zeta$ Puppis, obtained with the Reflection Grating Spectrometer on-board *XMM-Newton*. The spectrum exhibits bright emission lines of hydrogen-like and helium-like ions of nitrogen, oxygen, neon, magnesium, and silicon, as well as neon-like ions of iron. The lines are all significantly resolved, with characteristic velocity widths of order $1000 - 1500\,\mathrm{km\,s^{-1}}$. The nitrogen lines are especially strong, and indicate that the shocked gas in the wind is mixed with CNO-burned material, as has been previously inferred for the atmosphere of this star from ultraviolet spectra. We find that the forbidden to intercombination line ratios within the helium-like triplets are anomalously low for N VI, O VII, and Ne IX. While this is sometimes indicative of high electron density, we show that in this case, it is instead caused by the intense ultraviolet radiation field of the star. We use this interpretation to derive constraints on the location of the X-ray emitting shocks within the wind that are consistent with current theoretical models for this system.

**Key words.** Stars: individual: $\zeta$ Puppis – Stars: winds, outflows – Stars: early-type – X-rays: stars – Atomic processes – Line: formation

## 1. Introduction

The initial discovery of X-ray emission from O stars with the *Einstein Observatory* in the late 1970s (Harnden et al. 1979), sparked a vigorous field of research aimed at better understanding the production of hot gas in such systems. Most current models invoke hydrodynamic shocks resulting from intrinsic instabilities in the massive, radiatively driven winds from these stars (for a detailed review see Feldmeier et al. 1997). Support for this picture comes from the fact that the X-ray flux is not highly absorbed at low energies (Cassinelli & Swank 1983; Corcoran et al. 1993), which is expected if the X-ray emitting gas is distributed throughout the wind rather than in some form of hot corona in the outer atmosphere of the star. However, the X-ray observations to date have not been especially constraining for stellar wind models. This is primarily due to the low spectral resolution of the available nondispersive detectors, which has precluded the study of individual atomic features so crucial to the unambiguous determination of physical conditions in the shocked gas.

In this Letter, we present one of the first high resolution X-ray spectra of an early-type star, the O4Ief supergiant $\zeta$ Puppis, which we have obtained with the Reflection Grating Spectrometer (RGS) experiment on the *XMM-Newton* Observatory. $\zeta$ Pup is an excellent target for such work since it is the brightest O star in the sky, and has consequently been very well studied at longer wavelengths. In particular, Pauldrach et al. (1994) have developed a very detailed NLTE model of the atmosphere and wind of this star, constrained by high quality ultraviolet spectra from Copernicus and IUE. They find a mass loss rate of $\sim 5.1 \times 10^{-6}\,\mathrm{M_\odot\ yr^{-1}}$ and an effective temperature $\sim 42\,000\,\mathrm{K}$. The derived abundances indicate that the atmosphere is mixed with CNO-processed material, consistent with the theoretical picture of a highly evolved star near the end of core hydrogen burning. Hillier et al. (1993) found that the Pauldrach et al. model is consistent with the ROSAT X-ray spectrum of $\zeta$ Pup, but only if the X-ray emission arises in shocks distributed throughout the wind.

*Send offprint requests to*: skahn@astro.columbia.edu
⋆ Postdoctoral Researcher FNRS (Belgium)

At the very lowest energies ($\leq 200\,\mathrm{eV}$), they find that the emitting material must be $\geq 100\mathrm{R}_*$ away from the star. This is a consequence of the fact that in the Pauldrach et al. model, helium is mostly only singly ionized in the outer regions of the wind, so that the photoelectric opacity is very high at soft X-ray energies.

Our *XMM-Newton* RGS spectrum is dominated by broad emission lines of mostly hydrogen-like and helium-like charge states of nitrogen, oxygen, neon, magnesium, and silicon, and neon-like ions of iron. The data provide a number of important constraints on the nature and location of the X-ray emitting material in the $\zeta$ Pup wind. Of particular interest is the fact that we see a suppression of the forbidden line and enhancement of the intercombination line in the helium-like triplets of nitrogen, oxygen, and neon. We show that this is a natural consequence of the intense ultraviolet radiation field in the wind, and that it allows us to place constraints on the location of the X-ray emitting shocks relative to the star. Additional constraints come from the emission line velocity profiles. We show that the data are consistent with the predictions of the Pauldrach et al. model.

In section 2, we describe the details of the RGS observation, the nature of our data reduction and analysis, and the key observational features of the spectrum. In section 3, we consider the implications of our results for our understanding of $\zeta$ Pup, and of the X-ray emission from O stars in general.

## 2. Observations and Data Analysis

The RGS covers the wavelength range of 5 to 35 Å with a resolution of 0.05 Å, and a peak effective area of about $140\,\mathrm{cm}^2$ at 15 Å. $\zeta$ Pup was observed for 57.4 ks on 2000 June 8. The data were processed with the *XMM-Newton* Science Analysis Software (SAS). Filters were applied in dispersion channel versus CCD pulse height space to separate the spectral orders, and the source region was separated with a $1'$ spatial filter. The background spectrum was obtained by taking events from a region spatially offset from the source. The wavelengths assigned to the dispersion channels are based on the pointing and geometry of the telescope and are accurate to $\sim 0.008$ Å (see den Herder et al. 2000; this vol.). The effective area was simulated with a Monte Carlo technique using the response matrix of the instrument and the exposure maps produced by the SAS. Based on ground calibration, we expect the uncertainty in the effective area to be less than 10% above 9 Å and at most 20% for shorter wavelengths (den Herder et al. 2000). A fluxed spectrum, corrected for effective area, with the two first order spectra added together to maximize statistics, is presented in Fig. 1. There is a small discontinuity in the spectrum near the nitrogen Lyman $\beta$ line at 20.91 Å caused by a gap between two CCD chips. The spectrum was also extracted for analysis in XSPEC using standard SAS routines.

Due to a large solar flare event that occurred close to the time of the $\zeta$ Pup observation, all three EPIC detectors and the Optical Monitor on *XMM-Newton* were switched off while this source was observed. Thus, only data from RGS are available for analysis.

### 2.1. Light Curve

Previous ROSAT obervations of $\zeta$ Pup (Berghöfer et al. 1996) show evidence for a 16.67 h period of variability in the X-ray emission between 0.9 and 2.0 keV. We have extracted a light curve (Fig. 2) of the events in this energy range in the RGS data set. There is no significant observed variation on this time scale apparent to the eye, and the fit to a constant intensity yields $\chi^2_\nu = 0.9$. However, our upper limit to the percentage variation at this period is not inconsistent with the Berghöfer et al. detection.

### 2.2. Emission Line Intensities and Emission Measure Analysis

The spectrum displayed in Fig. 1 is composed almost entirely of emission lines, with a weak underlying continuum. The lines are all broadened, with characteristic velocity widths of order $1000\,\mathrm{km\,s}^{-1}$. In nitrogen, oxygen, and neon the He-like forbidden lines are very weak and the intercombination lines are bright. The line fluxes (Table 1) were measured by taking the integrated flux of the spectrum over the line and subtracting a corresponding amount of continuum flux. Lines that originate from the same ion and that are blended were evaluated as one complex (for example, the He-like triplets or the Fe XVII emission around 15 or 17 Å). The continuum strength was determined by taking the flux of a spectral region free of lines but near the line in question. In cases where this was not possible, the continuum strength was interpolated from the strength in other regions of the spectrum. Some of the measurements were complicated by the presence of overlapping lines. When possible, the flux of these other lines was estimated from the flux of lines originating from the same ion by comparing with line power ratios.

We calculated the emission measure (see Fig. 3) for each ion assuming solar abundances (Anders & Grevesse 1989) and a temperature given by the temperature of formation for the dominant lines from that charge state. The emission measure is

$$EM = F_{\mathrm{line}} \frac{4\pi d^2}{P_{\mathrm{line}} A f_{\mathrm{i}}} \qquad (1)$$

where $F_{\mathrm{line}}$ is the observed flux in the line, $d$ is the distance to the source, $P_{\mathrm{line}}$ is the line power, $A$ is the elemental abundance, and $f_{\mathrm{i}}$ is the ion fraction evaluated at the temperature of formation. We used line powers from the APEC code (Smith & Brickhouse 2000), which includes ion fractions from Mazzotta et al. (1998). We take $d = 450\,\mathrm{pc}$ (Schaerer et al. 1997). The line fluxes must be corrected for interstellar absorption, although this is a minor effect. We take $N_{\mathrm{H}} = 10^{20}\,\mathrm{cm}^{-2}$ (Chlebowski et al. 1989) and we use cross sections from Morrison & McCammon (1983).

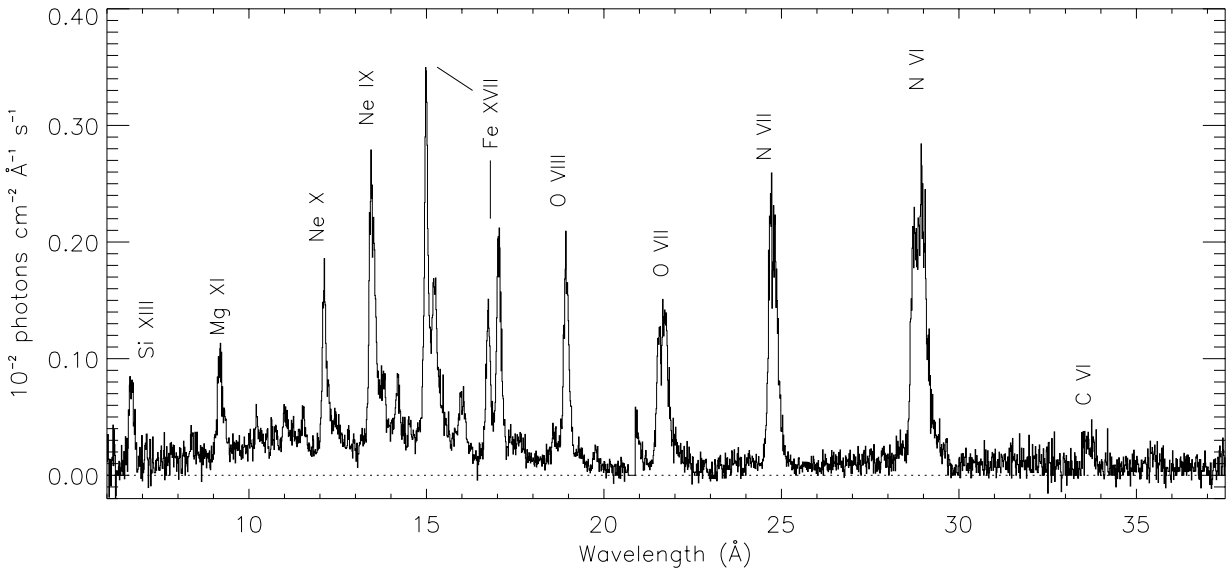


**Fig. 1.** First order background subtracted spectrum. It has been corrected for the effective area of the instrument.

We find that the emission measures derived from the nitrogen emission lines are at least an order of magnitude greater than those for carbon and oxygen, which both have temperature of formation ranges that overlap with that of nitrogen. This indicates that the ratios $A_{\rm N}/A_{\rm O}$ and $A_{\rm N}/A_{\rm C}$ are substantially higher than solar, even allowing for a factor of two uncertainty due to the crudeness of the emission measure analysis. This result is consistent with the inference of atmospheric abundances by Pauldrach et al. (1994), based on their analysis of UV spectra. It indicates that the wind material in ζ Pup has been significantly mixed with matter that has undergone CNO burning in the stellar interior.

The emission measure expected for a smooth, spherically symmetric wind with parameters appropriate to ζ Pup is $EM = 6.5 \times 10^{60}{\rm cm}^{-3}$. The fact that we find EMs that are lower by 4 to 5 orders of magnitude implies that only a small fraction of the wind material is heated to X-ray emitting temperatures.

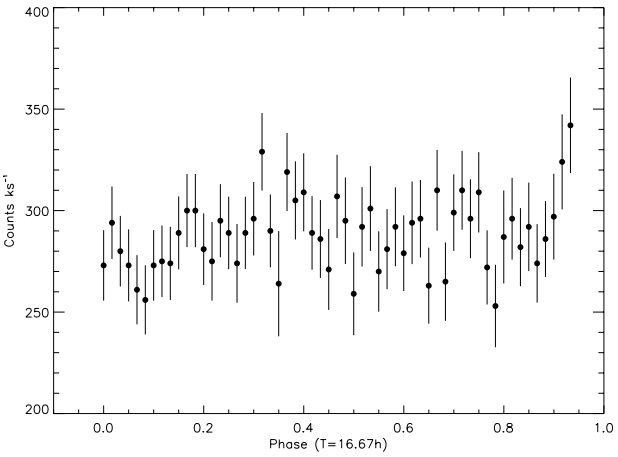


**Fig. 2.** Light curve of first order events in the range 6.2 to 13.8 Å, corresponding to 0.9 to 2.0 keV. Events from both instruments have been binned together. The time dependence is plotted as a function of the 16.67 hr period reported in Berghöfer et al.

### *2.3. Continuum emission analysis*

The continuum emission has a very low intensity relative to the bright line emission. To ensure that the continuum that we see in the spectrum is real, and not, for example, an artifact of faulty background subtraction, we plotted the first order events in a region free of emission lines as a function of their spatial distribution in the cross-dispersion direction, without subtracting the background. The peak at the location of the source spectrum is clearly visible, and indicates the presence of true continuum, well above background. The detected continuum also significantly exceeds the scattered light contribution from the ensemble of detected emission lines.

We looked for evidence of discrete photoelectric absorption edges in the continuum. Although there are no edges evident, the constraints are weak due to the low strength of the continuum emission. The upper limits on the optical depths are given in Table 2. These upper limits are incompatible with the detection of a strong edge feature near 0.6 keV reported by Corcoran et al. (1993), but that is perhaps not surprising, considering the complexity of the spectrum and the low spectral resolution of their measurements.

The continuum is so weak that it is difficult to ascertain its overall shape, especially in the region from 8 - 17 Å where there are many lines. We tried fitting with

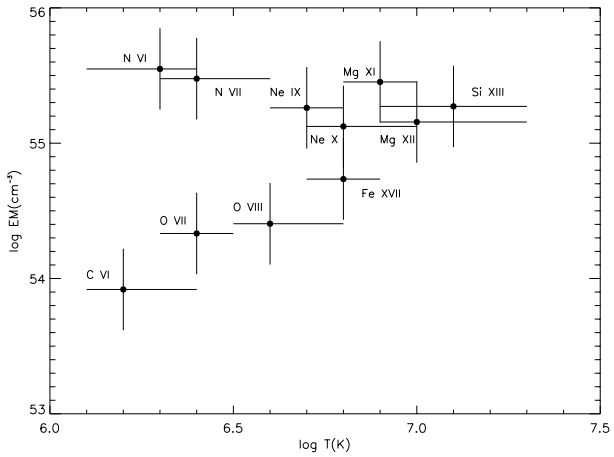


**Fig. 3.** Emission measure calculated from each line as a function of $T_{\rm form}$. The horizontal error bars indicate the temperature range over which $P_{\rm line} f_{\rm i}$ is at least half its maximum value. Solar abundances are assumed.

**Table 1.** Measured fluxes for prominent emission lines with rest wavelengths in Å.

| Line | Flux (photons cm$^{-2}$ s$^{-1}$) |
|---|---|
| Si XIII (6.65, 6.69, 6.74) | $(1.1 \pm 0.4) \times 10^{-4}$ |
| Mg XII (8.42) | $(4.1 \pm 2.8) \times 10^{-5}$ |
| Mg XI (9.17, 9.23, 9.31) | $(2.0 \pm 0.7) \times 10^{-4}$ |
| Ne X (12.13) | $(1.8 \pm 0.7) \times 10^{-4}$ |
| Ne IX (13.45, 13.55, 13.70) | $(5.0 \pm 1.0) \times 10^{-4}$ |
| Fe XVII (15.01, 15.26) | $(7.4 \pm 0.7) \times 10^{-4}$ |
| Fe XVII (16.78, 17.05, 17.10) | $(4.7 \pm 0.8) \times 10^{-4}$ |
| O VIII (18.97) | $(3.50 \pm 0.22) \times 10^{-4}$ |
| O VII (21.60, 21.80, 22.10) | $(5.1 \pm 0.4) \times 10^{-4}$ |
| N VII (24.78) | $(6.4 \pm 0.5) \times 10^{-4}$ |
| N VI (28.78, 29.08, 29.53) | $(1.13 \pm 0.11) \times 10^{-3}$ |
| C VI (33.74) | $(6.4 \pm 2.8) \times 10^{-5}$ |

**Table 2.** Upper limits on the strengths of the K-edges of Ne, O, and N.

| Edge | Wavelength (Å) | Upper limit on $\tau_0$ |
|---|---|---|
| Ne X | 9.10 | 0.5 |
| Ne IX | 10.37 | 0.5 |
| O VIII | 14.23 | 0.2 |
| O VII | 16.78 | 0.3 |
| N VII | 18.59 | 0.5 |
| N VI | 22.46 | 0.5 |

a bremsstrahlung model in XSPEC, but the results were inconclusive.

### 2.4. He-like triplet ratios

The forbidden to intercombination line ratios, $R = f/i$, for helium-like oxygen and neon were obtained by fitting in XSPEC. In each case, we fit a gaussian to the Ly$\alpha$ line of the respective element, and used that profile for each of the three components in the He-like triplet. We also take into account both the low level continuum and lower flux lines in the near vicinity. For Ne IX we find R = $0.34 \pm 0.11$ and for O VII we find R = $0.19 \pm 0.08$. The fit to Ne IX is shown in Fig. 4. These values are well below the expected values for low density plasmas in collisional equilibrium (see Mewe et al. 2000). A similar analysis did not work very well for the N VI He-like triplet because of the complexity of both the Ly$\alpha$ and He-like profiles for that element. Nevertheless, it is clear from the data that the forbidden line is strongly suppressed for N VI as well. The Si XIII and Mg XI triplets are too blended to allow the forbidden line and intercombination line to be quantitatively separated. Again, it is clear from the data that the Mg XI forbidden line is suppressed, although not as strongly as for Ne IX.

The conversion of forbidden line to intercombination line emission in high density plasmas is a well known effect. However, this can also occur at much lower densities if the plasma is exposed to a strong UV radiation field (Mewe & Schrijver 1978). To produce a low $R$ ratio, electrons populating the 2 $^3S_1$ state must be excited into the 2 $^3P$ state. The state 2 $^3S_1$ is metastable, but it is easily populated at collisional equilibrium temperatures, and the corresponding emission line intensity is normally strong. When the excitation rate to the 2 $^3P$ levels becomes comparable to the decay rate to the ground state, the forbidden line is suppressed. In a high density plasma, this occurs because the collisional excitation rate from 2 $^3S_1$ to 2 $^3P$ competes effectively with radiative decay. However, since this is a dipole transition, it can also be photoexcited if the ambient UV flux at the appropriate wavelength is sufficiently high. To calculate the photoexcitation rate, we estimated the emission from ζ Pup for the frequencies of the 2 $^3S_1$ to 2 $^3P$ transitions for N, O, Ne, Mg, and Si. We assumed a blackbody spectrum with $T_{\rm eff}$ = 42 000K (Pauldrach et al. 1994). The rate of photoionization is given by $R_{\rm PE} = F_\nu \frac{\pi e^2}{mc} f$, where $f$ is the oscillator strength. We used oscillator strengths from Cann and Thakkar (1992) and Sanders and Knight (1989). The flux is given by $F_\nu = 2\pi(1 - \sqrt{1 - (\frac{R_*}{R})^2}) I_\nu$, where $I_\nu$ is the specific intensity for the blackbody.

We used the archived IUE UV spectrum of ζ Pup in addition to the Copernicus UV spectrum (Morton and Underhill 1977) to assess the validity of our blackbody model for the UV emission from the photosphere. We compared the measured flux at the wavelengths of the 2 $^3S_1$ to 2 $^3P$ transitions for N VI, O VII, and Ne IX to the flux predicted by the blackbody model. After correcting the measured flux for absorption, these agree to within a factor of two. Since the critical radius where $R_{\rm PE} = R_{\rm decay}$

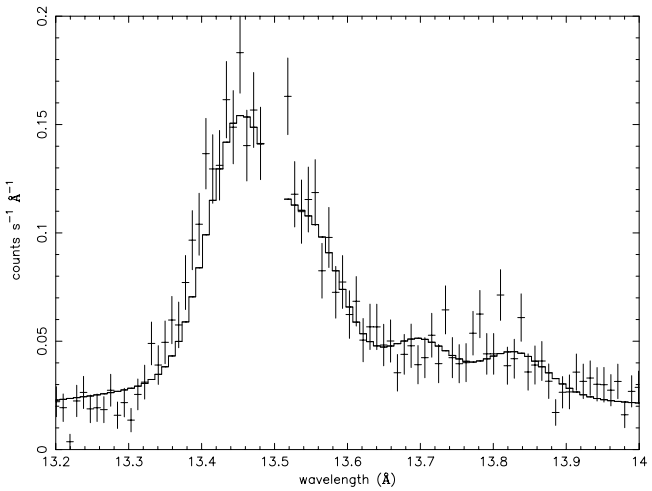


**Fig. 4.** The Ne IX triplet with best fit model. Only RGS 2 data are shown for clarity, but both were used in the fit. There is also a Fe XVII line at 13.825 Å. The rest wavelengths of the three lines are at 13.45 Å (r), 13.55 Å (i), and 13.70 Å (f).

depends approximately on $\sqrt{F_\nu}$, the radii we calculate are valid to within a factor of $\sqrt{2}$. The measured UV spectra also indicate that there is negligible optical depth in these lines due to the wind. This is expected since these are excited state transitions, and since the helium-like plasma only represents a very small fraction of the wind.

In Table 3 we list the decay rates of 2 $^3S_1$ and the photoexcitation rates from 2 $^3S_1$ to 2 $^3P$ evaluated at the photosphere. It is clear from this calculation that the forbidden line suppression we observe is in fact due to photoexcitation from $\zeta$ Pup's high UV flux, and not due to collisional excitation at high densities, as long as the emitting regions are close enough that the UV is not sufficiently diluted. We can thus place constraints on the location of shock formation for each of the observed lines. Since the forbidden lines in N, O, and Ne are strongly suppressed, the emission must occur at radii smaller than the radii at which the photoexcitation and decay rates are equal (the critical radius). Since Mg XI has a somewhat suppressed forbidden line, its emission probably occurs near the critical radius. The emission from Si must occur farther out than the critical radius.

### 2.5. Line profile analysis

The projected velocity ($v_{\rm p}$) profile for a thin spherical shell (with a single radial velocity) is flat, or $\frac{dI}{dv_{\rm p}} = (\text{const.})$. We expect the emission line profile to appear as a convolution of the radial emission intensity with this flat projected velocity profile. The velocity of each shell is given as a function of radius by the conventional $\beta$-model: $v(r) \approx v_\infty(1 - r_0/r)^\beta$ (Lamers & Cassinelli 1999) where $\beta \approx 0.8$ and $r_0 \approx R_*$. Lines formed at larger radii will therefore appear broader than lines formed close to the star. Furthermore, lines originating from larger radii

**Table 3.** Comparison of photoexcitation and decay rates of the 2 $^3S$ state. Decay rates are from Drake (1971).

| Ion | Decay Rate $2\ ^3S \rightarrow 1\ ^1S$ ($s^{-1}$) | Photoexcitation Rate ($R = R_*$) $2\ ^3S \rightarrow 2\ ^3P$ ($s^{-1}$) | Radius at which $R_{\rm PE} = R_{\rm decay}$ ($R_*$) |
|---|---|---|---|
| Si XIII | $3.56 \times 10^5$ | $4.83 \times 10^6$ | 2.7 |
| Mg XI | $7.24 \times 10^4$ | $7.36 \times 10^6$ | 7.1 |
| Ne IX | $1.09 \times 10^4$ | $1.11 \times 10^7$ | 22.6 |
| O VII | $1.04 \times 10^3$ | $1.66 \times 10^7$ | 89 |
| N VI | $2.53 \times 10^2$ | $1.99 \times 10^7$ | 198 |

**Table 4.** Velocity widths and shifts of the Lyman $\alpha$ lines.

| Ion | Velocity shift ($km\,s^{-1}$) | Velocity width ($km\,s^{-1}$) |
|---|---|---|
| Ne IX | $250 \pm 125$ | $940 \pm 150$ |
| O VII | $400 \pm 80$ | $1230 \pm 80$ |
| N VI | $0 \pm 60$ | $1370 \pm 100$ |

are formed over a region with a small velocity gradient. Therfore, we expect these lines to appear more flat-topped than lines originating closer to the star. This is apparent in the observed Ly$\alpha$ lines, which are plotted in velocity space in Fig. 5. The N VII peak is noticeably broader and has a substantially different shape than the other peaks in the plot. It also shows evidence for resolved, discrete structure, given the resolution of the instrument. Note that other lines overlap with the Ne X line; it does not have a red shoulder.

In Table 4 we list the shifts in the line centroids and the line widths in velocity space for Ne X, O VIII, and N VII. The fit to N VII is poor due to the complex structure in the line profile.

## 3. Discussion

The RGS spectrum we have presented provides very strong confirmation for a number of key aspects of conventional models of X-ray emission from early-type stars in general, and for $\zeta$ Pup in particular. The emission is dominated by broad emission lines indicative of hot plasma that is flowing outward with the wind. We do not see evidence for strong attenuation at low energies, which confirms that the X-ray emitting regions are not concentrated at the base of the wind, but instead are distributed out to large radii. These very simple results agree well with the predictions of wind instability models.

As we have shown, the suppression of the forbidden lines in the He-like triplets of low Z elements allows us to derive upper limits to the radii of the emitting shocks in each case. It is interesting to compare these values with Fig. 1 of Hillier et al. (1993), which is a plot of the radius

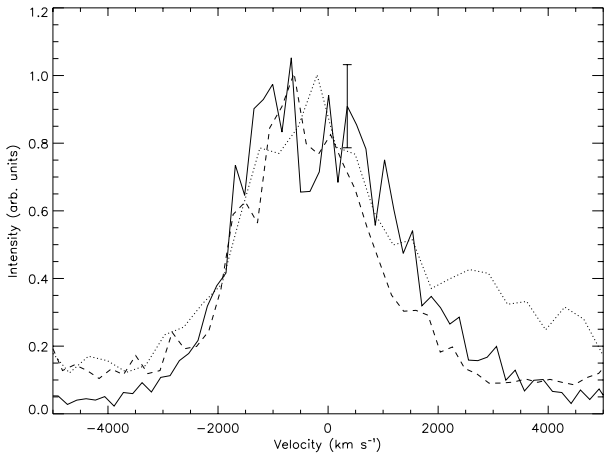


**Fig. 5.** Ly $\alpha$ lines in velocity space. Nitrogen is the solid line, oxygen is dashed, and neon is dotted. The intensities have been renormalized for comparative purposes. The error bar is representative for the nitrogen line. Note the discrete structure in the nitrogen peak. The shoulder on the Ne X line is not a velocity feature; it is an emission line from Fe XVII.

at which optical depth unity is reached in the wind as a function of X-ray energy for the NLTE model of $\zeta$ Pup calculated by Pauldrach et al. (1994). At the energies of the N VI, O VII, Ne IX, Mg XI, and Si XIII lines, unit optical depth is achieved at 22, 23, 9, 3.5, and 2.5 stellar radii, respectively, in this model. These values are quite compatible with both our derived upper limits for N VI, O VII, Ne IX, and Mg XI, and our derived lower limit for Si XIII. Since the density in the wind drops off like $r^{-2}$, and the emissivity is proportional to $n^2$, we expect radii characteristic of the smallest radius at which the overlying wind is still transparent to the respective line, in each case. Our results are consistent with this expectation.

Further support for this picture comes from the observed velocity profiles. The higher Z lines have characteristic widths $\sim 1000\,\mathrm{km\,s^{-1}}$, whereas the N VII line is distinctly broader. The terminal velocity in the $\zeta$ Pup wind is $2260\,\mathrm{km\,s^{-1}}$ (Groenewegen et al. 1989), so the higher Z lines are most likely emitted at only a few stellar radii, whereas N VII can come from considerably further out.

We have shown that the respective line intensities are suggestive of significant enhancements of the nitrogen abundance relative to carbon and oxygen, as one would expect for CNO-processed material. This, again, agrees well with the Pauldrach et al. model. Meynet & Maeder (2000) recently presented new evolutionary models for rotating single stars. They found that rotational mixing produces a significant surface helium and nitrogen enhancement. Meynet & Maeder suggested that stars with enhanced He-abundances and large projected rotational velocities are natural descendants of very fast rotating main-sequence stars. In these stars, the chemical enrichment at the surface is very fast and as a result of the strong rotational mixing the chemical structure of these stars could be near homogeneity. With its large projected rotational velocity of $v \sin i \simeq 203\,\mathrm{km\,s^{-1}}$ (Penny 1996), $\zeta$ Pup most probably falls into this category.

*Acknowledgements.* We acknowledge useful comments from the referee, M. Corcoran, which significantly improved the presentation of this paper. This work is based on observations obtained with *XMM-Newton*, an ESA science mission with instruments and contributions directly funded by ESA Member States and the USA (NASA). The Columbia University team is supported by NASA. SRON is supported by the Netherlands Foundation for Scientific Research (NWO). GR and JMV acknowledge support by the SSTC-Belgium under contract P4/05 and by the PRODEX XMM-OM Project. JC acknowledges the support of a NASA Graduate Student Researchers Program Fellowship.

## References

Anders E., Grevesse N., 1989, Geochimica et Cosmochimica Acta 53, 197
Berghöfer T.W., Baade D., Schmitt J.H.M.M., Kudritzki R.-P., Puls J., Hillier D.J., Pauldrach A.W.A., 1996, A&A 306, 899
Cann N.M., Thakkar A.J., 1992, Phys. Rev. A 46, 9, 5397
Cassinelli J.P., Swank J.H., 1983, ApJ 271, 681
Chlebowski T., Harnden F. R., Sciortino S., 1989, ApJ 341, 427
Corcoran M. F., Swank J. H., Serlemitsos P. J., Boldt E., Petre R., Marshall F. E., Jahoda K., Mushotzky R., Szymkowiak A., Arnaud K., Smale A. P., Weaver K., Holt S. S., 1993, ApJ 412, 792
den Herder, J.W., et al., 2000, this volume.
Drake G.W.F., 1971, Phys. Rev. A 3, 908
Feldmeier A., Kudritzki R.-P., Palsa R., Pauldrach A.W.A., Puls J., 1997, A&A 320, 899
Groenewegen M.A.T., Lamers H.J.G.L.M., 1989, A&AS 79, 359
Harnden F.R. Jr., Branduardi G., Elvis M., et al., 1979, ApJ 234, L51-54
Hillier D.J., Kudritzki R.-P., Pauldrach A.W.A., Baade D., Cassinelli J.P., Puls J., Schmitt J.H.M.M., 1993, A&A 276, 117
Lamers H.J.G.L.M., Cassinelli J.P., 1999, Introduction to Stellar Winds
Mazzotta P., Mazzitelli G., Colafrancesco S., Vittorio N., 1998, A&AS 133, 403
Mewe R., Schrijver J., 1978, A&A 65, 99
Mewe R., Porquet D., Raassen A.J.J., Kaastra J.S., Dubau J., 2000, in preparation
Meynet G., Maeder A., 2000, A&A 361, 101
Morton D.C., Underhill A.B., ApJS 33, 83
Morrison R., McCammon D., 1983, ApJ 270, 119
Pauldrach A.W.A., Kudritzki R.P., Puls J., Butler K., Hunsinger J., 1994, A&A 283, 525
Penny L.R., 1996, ApJ 463, 737
Sanders F. C., Knight R. E., 1989, Phys. Rev. A 39, 9, 4387
Schaerer D., Schmutz W., Grenon M., 1997, ApJ 484, L153
Smith R., Brickhouse N., 2000, Astrophysical Plasmas: Codes, Models, and Observations, Proceedings of the conference held in Mexico City, October 25-29, 1999, Eds. Jane Arthur, Nancy Brickhouse, and José Franco, Revista Mexicana de Astronomía y Astrofísica (Serie de Conferencias), Volume 9, p. 134-136